


Article

Study of Excitation Characteristics of Traction Machine/Drive Systems

Wenying Jiang , Qiqi Guo and Zhen Zhang

Center for More-Electric-Aircraft Power System, Nanjing University of Aeronautics and Astronautics, Nanjing 211106, China; 15195891668@163.com (Q.G.); zhenxwls@163.com (Z.Z.)

* Correspondence: wenying.jiang@nuaa.edu.cn; Tel.: +86-187-0514-5035

Received: 21 November 2019; Accepted: 25 December 2019; Published: 27 December 2019



Abstract: In order to accurately evaluate the performance of a traction machine/drive system, it is necessary to have an accurate excitation source which considers current harmonics. In this paper, four machine/drive systems with different excitation sources have been modeled, simulated, and studied to evaluate the effects on permanent magnet synchronous machines (PMSMs) from different perspectives. In Model I, the excitation is an ideal sinusoidal current source with no harmonics. Model II is excited by an ideal sinusoidal voltage source regardless of the pulse width modification's (PWM's) influence. Model III takes into account the influence of current harmonics under space vector pulse width modulation (SVPWM) control. Model IV is based on the equivalent circuit extraction (ECE) model (a look-up table motor model). We simulate these four models and study the characteristics of the excitation sources, based on the observations of current harmonics, torque, electromagnetic force, computation time, and efficiency. Experiments are also conducted to show that Model III allows the most precise study of the considered system. Model IV is a good substitution, providing similar results with a shorter running time.

Keywords: PMSM; excitations; current harmonics; ECE; SVPWM

1. Introduction

With the advantages of high efficiency and high torque density, permanent-magnet synchronous motor drive systems are widely adopted in many fields, such as in household electric appliances, industrial robots, electric transportation, etc. [1–3]. In the automotive industry, electric vehicles (EV) have most recently attracted the interests of many companies, who have developed permanent magnet synchronous motors with superior performance for EVs. The Nissan Leaf has the interior permanent magnets arranged in a ∇ -shape, which achieves a superior balance of torque and power [4]. The inverter integrated with the motor in Nissan Leaf reduces weight and volume, and thus increases torque density [5]. Hyundai launched the Hyundai Sonata motor, which has a fractional slot concentrated winding motor in 2012 [6]. The Chevrolet Bolt has the hairpin winding motor with a high copper space factor and high efficiency [7]. Without any doubt, the design of the electric machine is essential for EVs to have a long range and a high level of comfort.

In the design of sinusoidal permanent-magnet synchronous traction motors, a commonly used analysis method is to apply the excitation of sinusoidal current to the motor winding in the finite element simulation to observe the electromagnetic characteristics of the motor. As a widely adopted method in both industrial applications and academic research, finite element simulations are considered to have precise results; however, the excitation model is not accurate enough to calculate the losses and electromagnetic force. The losses are important for the thermal simulation of the motor, and electromagnetic force is essential to acquire the noise, vibration, and harshness (NVH) of the motor drive system. It is thus very important to have more accurate excitation models. Considering the

actual control environment, in which the motor windings are connected to the inverter and excited by the voltage source, the space vector pulse width modulation (SVPWM) technique is thus employed among various modulation techniques, due to its superior performance in bus voltage utilization and overall efficiency [8–10]. Current harmonics generated by pulse width modulation (PWM) cannot be ignored when using an SVPWM control strategy because it leads to the increase of the losses, torque ripple, vibration, and noises [11–17]. In particular, in [11,12], it is shown that the eddy-current loss of the magnets increases significantly, caused by high-order carrier harmonics of the inverter, bringing the risk of irreversible demagnetization of the magnets. In [13], the authors calculate the eddy-current loss of permanent-magnet motors driven by PWM inverters, and conclude that the magnets' eddy-current loss is mainly produced by the carrier harmonics. Reference [14] introduces that the amplitude of harmonic currents has little effect on the average torque of permanent magnet synchronous machines (PMSMs), and the torque ripple gets larger as the amplitude of the harmonic currents gets larger. In [15], the EV motor driven by an inverter has a large PWM carrier harmonic iron loss in the low-torque region. References [16,17] show that the electromagnetic noise derives mainly from the electromagnetic force, caused by the component in the current harmonics under PWM. Hence, current harmonics of the excitation sources must be included to increase the accuracy of the model of the motor drive system.

In order to acquire the current harmonics under PWM control, the authors of [18] derive the calculating formula for current harmonics. Note that the formula works with the dq axis inductance L_d and L_q , which vary for different operating points. To analyze the entire operating region of the motor, the current harmonics of each working point have to be calculated one by one. It can cost even one week to simulate just one single working point, which makes it impossible to be applied in traction machine applications. For many traction machine designs, this is not necessary. A rapid and accurate method for current harmonics evaluation is thus proposed for the traction machine/drive system [19]. Based on the previous model, this new method firstly constructs an equivalent circuit extraction (ECE) (a look-up table) and uses ECE to simulate the entire operating region of the motor, which avoids time-consuming co-simulation for every operating point, and thus saves much time. The above two methods both include current harmonics in the excitation sources, which highly increases the accuracy of the excitation model. It is therefore very interesting and necessary to thoroughly study their excitation characteristics in a motor drive system model.

Motivated by this, we propose the corresponding two-motor drive system models based on the above two different excitation sources. To better evaluate the characteristics of different excitations, we also present two other models. One is a fundamental model driven by an ideal current source with no harmonics, and the other is a typical model driven by an ideal voltage source. We then compare these four models of different excitation characteristics to see their differences in modeling of the complete motor drive system. Based on an ideal current source, Model I is widely used to simulate machine performance, since it is capable of accurately predicting machine torque production, considering the nonlinear properties of the materials. However, the actual excitation of the motor winding is a voltage source. Model II is thus excited by an ideal sinusoidal voltage source regardless of the PWM's influence, which is especially useful in predicting low-order current harmonics. Model III takes into account the influence of current harmonics under SVPWM control, providing more details of the excitation sources. Model IV uses an ECE model (look-up table model) which is established on the basis of Model III. It is a trade-off between the model accuracy and simulation time. To further verify the simulation results from different models, we also build an experimental platform to compare with the experimental results, which makes our work more convincing. The results provide sufficiently rich references for selecting suitable excitations for different purposes.

The main contribution of this paper is the evaluation of the influences of different excitations on the overall motor performance by considering the current harmonics in the excitation sources. The excitation characteristics and the corresponding performance of the motor drive system are fully investigated. We establish and compare four models of different excitations. Based on the

observations of the characteristics of torque, electromagnetic force, computation time, and efficiency, their interconnections with the current harmonics are further analyzed. Experiments are also conducted to verify the results. The results from this research not only provide references for model selection based on different applications, but also provide strong evidence and an innovative perspective for further research of NVH characteristics of the motor drive system, which directly reflect the comfort levels and battery performances of EVs.

The remainder of this paper is organized as follows. Section 2 introduces the four different models with different excitations and analyzes the characteristics of their current harmonics. Section 3 introduces the motor which we use to verify, test, and compare the models in this paper. Section 4 compares the models with both simulated and experimental results. Section 5 concludes this paper.

2. Illustration of the Four Machine/Drive Models of Different Excitations and Their Characteristics

In this section, we introduce the principles and the establishment of four models of different excitations (ideal sinusoidal current source excitation model, ideal sinusoidal voltage source excitation model, practical simulation model considering PWM and practical simulation model considering ECE). Based on the models, we present their excitation characteristics.

2.1. Illustration of Model I

Model I is a 2-D finite element (FE) electromagnetic model of the machine. The structure of Model I is shown in Figure 1. The ideal sinusoidal current source is fed into the finite element model. In order to obtain the performance of the motor in the entire operation region, an MTPA control strategy is used in the constant torque region of the motor, and flux-weakening control is used in the constant power region of the motor. Model I is often used to quickly validate the major performances of motor designs.

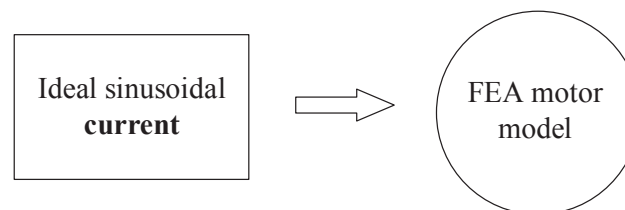


Figure 1. The block of Model I.

2.2. Illustration of Model II

In Model II, the motor is excited by an ideal sinusoidal voltage source to analyze the electromagnetic characteristics of the motor. The structure of Model II is shown in Figure 2.

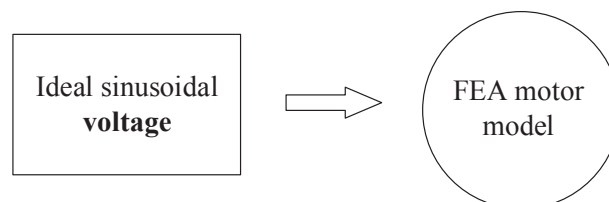


Figure 2. The block of Model II.

The amplitude of the voltage source is set based on the fundamental amplitude of the phase voltage in Model I. To guarantee that the machine works stably at the target operating point (ω_0, T_0) , the load torque is adjusted according to the speed, as expressed in the following equations [20]. When the motor speed is lower than the target speed, it is increased by setting a larger load torque. When

the motor speed is higher than the target speed, a small load torque is set to reduce the motor speed. When the motor speed is equal to the target speed, the load torque is the value of the target torque.

$$T_L = -\frac{T_0}{\omega_0} \cdot \omega - \frac{T_0}{\omega_0} \cdot (\omega - \omega_0) \cdot k, \omega < \omega_0 \quad (1)$$

$$T_L = -\frac{T_0}{\omega} \cdot \omega_0 - \frac{T_0}{\omega_0} \cdot (\omega - \omega_0) \cdot k, \omega \geq \omega_0, \quad (2)$$

where T_0 and ω_0 are the electromagnetic torque and angular speed, respectively, at the target operating point; T_L and ω are the real-time load torque and rotor angular speed, respectively; k is set to start the motor.

2.3. Illustration of Model III

In Model III, the motor model is linked to a vector control system to establish co-simulation. In this model, the speed is set to be constant and the dq axis currents i_d and i_q are controlled to produce the objective torque. A look-up table is often used to locate the required dq axis currents i_d and i_q according to the reference torque and speed. The configuration of Model III is shown in Figure 3, where i_A , i_B , and i_C are the three phase currents. i_α and i_β are currents in the stationary coordinate system. i_d^* , i_q^* , u_d^* , and u_q^* are the reference values of the dq axis currents and voltages, respectively. u_α^* and u_β^* are the reference values of the voltages in the two-phase stationary coordinate system. The SVPWM method is used to generate the switching signal.

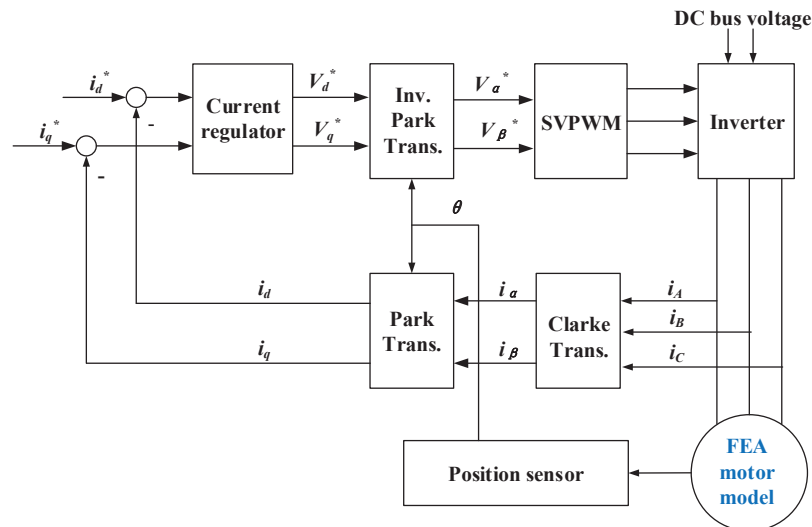


Figure 3. The configuration of Model III.

The current regulator of the machine drive is shown in Figure 4. It adopts a complex vectors model which is not sensitive to parameters for achieving good dynamic performances [21,22]. In Figure 4, ω_e is the electric angular velocity and p is the derivative operator. The proportional integral coefficient of dq axes K_{pd} , K_{pq} , K_{id} , and K_{iq} can be calculated by Equations (3) and (4), respectively, where BW_c is the bandwidth of the current loop. PI parameters under different working points need to be adjusted to obtain the performance over the entire operational area. For each working point to be analyzed, the dq axis current and rotation speed are set in Model III.

$$K_{pd} = L_d \cdot BW_c, K_{pq} = L_q \cdot BW_c \quad (3)$$

$$K_{id} = -\frac{R}{L_d}, K_{iq} = -\frac{R}{L_q} \quad (4)$$

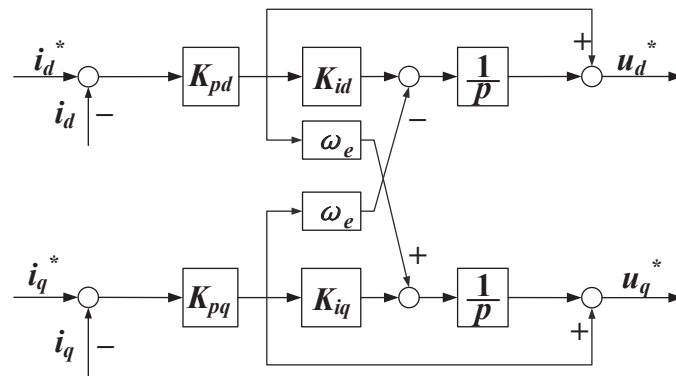


Figure 4. Illustration of the current regulator.

2.4. Illustration of Model IV

In Model IV, the establishment process has two steps. The first step is to establish the ECE model, and the second step is to establish the co-simulation in the drive system and the ECE model. Model IV has the same configuration as Model III, except that the FEA model is replaced by the ECE model. The ECE model is an intelligent look-up table that is built by recording machine parameters at different operating points. The establishment of the look-up table is shown in Figure 5. The look-up table includes the flux linkage data, which are obtained from the combinations of different i_d , i_q , and rotor positions. Then, according to the set values of i_d , i_q , and the rotor position, the look-up table is formed by collecting FEA results for each operating point.

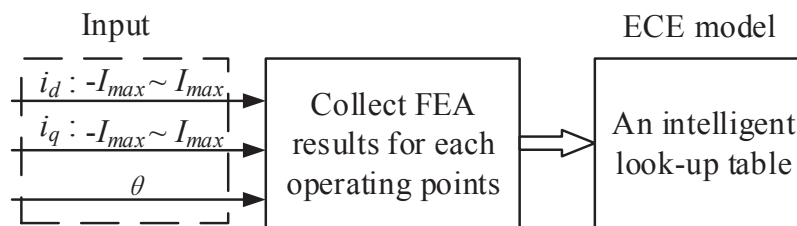


Figure 5. Flowchart of the setup of the equivalent circuit extraction (ECE) motor model.

Since the motor parameters extracted by the look-up table are the flux linkage of the motor, and the flux linkage is independent of the speed, the motor speed has no influence on the establishment of the look-up table in the process of parameter extraction. In addition, the look-up table model established by analyzing and extracting parameters of the motor at any speed can be used to analyze the characteristics of the entire motor operation area.

Then, Model IV is constructed by retaining the co-simulation configuration as in Model III, but replacing the PMSM FEA model with the ECE model, which is described in Figure 6. To apply Model IV, the reference current i_d^* and i_q^* is firstly set for each working point, the motor is set to a constant speed, and the moment of inertia and load torque are set.

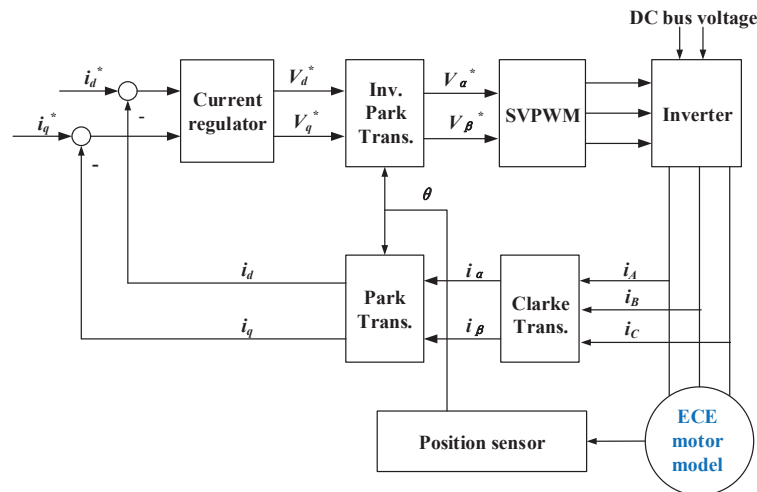


Figure 6. Illustration of Model IV.

2.5. Characteristics of Excitations in the Four Models

Based on the above models, we now analyze the characteristics of the excitations. In Figure 1, although Model I can be used to quickly evaluate major machine performance, it is excited by an ideal sinusoidal current without any current harmonics.

For Model II, the machine is excited by a sinusoidal voltage source in Figure 2; as in the actual operation of the machine, the windings are connected to a voltage source inverter. Thus, current harmonics are inevitably generated. It is especially good at predicting low-order current harmonics.

Model III considers the actual running state of the motor, and it thus fits the actual simulation very well and with high accuracy. It can also estimate the low-order components of the current harmonics. On the other hand, it is very time consuming when applied for evaluating traction machine/drive system performance over the whole operating region.

Differently from Model III, Model IV adopts an ECE motor model (see Figure 6), which significantly shortens the simulation time while maintaining some of the characteristics of the current harmonics of Model III. It is actually a trade-off between model accuracy and simulation time.

To further investigate the overall performance of the four models, we then design a traction motor as our target machine, and carry out simulations and experiments based on the target machine. From the simulation and experimental results, we analyze and further examine the excitation characteristics of different models.

3. The Target Machine and Model Settings

In this section, we design a 48-slot/8-pole interior permanent-magnet (PM) machine model as the target machine, in order to verify and compare the four models introduced in Section 2. We also set the parameters of these four models when the motor is running at the rated speed and peak power point (2200 r/min, 262 Nm). The construction of our experimental platform is also presented.

3.1. The Target Motor

A 48-slot/8-pole interior PM machine as the target machine is shown in Figure 7. The model has continuous 30 kW and peak 60 kW power output with a rated speed of 2200 r/min and maximum speed at 8000 r/min. The details of the motor parameters are shown in Table 1. In order to analyze and compare different drive models and excitation sources, the four traction machine/drive models are constructed according to this motor.

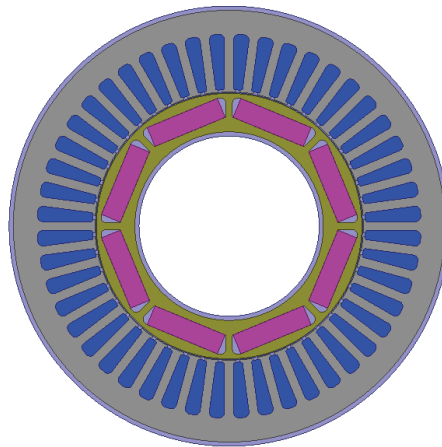


Figure 7. The configuration of the target machine.

Table 1. Parameters of the target machine.

Parameters	Value
Outer diameter of stator	205 mm
Inner diameter of stator	128 mm
Air gap length	0.75 mm
Stator stack length	127 mm
Number of slots	48
Number of pole pairs	4
Peak power	60 kW
Maximum speed	8000 rpm

3.2. Parameter Settings for the Four Models

In Model I, the original position of the rotor is initialized manually so that axis d and axis A overlap at the very beginning in the finite element simulation software. The current amplitude of the ideal current excitation is 300 A, and the electromagnetic characteristics at the rated speed point are simulated.

In Model II, the motor windings are excited by an ideal sinusoidal voltage source. The voltage amplitude of the ideal voltage source at the point of 2200 r/min and 262 Nm is 211.7 V. According to the Equations (1) and (2), the load torque is adjusted according to the speed, as expressed in Equations (5) and (6):

$$T_L = -1.137 \cdot \omega - 1.137 \cdot (\omega - 230.38) \cdot 10, \omega < 230.38 \quad (5)$$

$$T_L = -\frac{60360.47}{\omega} - 1.137 \cdot (\omega - 230.38) \cdot 10, \omega \geq 230.38. \quad (6)$$

In Model III, the motor model is built to establish co-simulation. The speed is set as 2200 rpm and the dq axis currents i_d and i_q are respectively -173.32 A and 230 A. The bus voltage is set at 540 V and the switching frequency is 5 kHz.

In Model IV, the parameters used to collect the ECE model are as follows: The steps of both i_d and i_q are 10 A, and both i_d and i_q are from -300 A to 300 A; the step of the rotor position is 0.75 degrees, which means that the step of the electrical position is 3 degrees. Then, Model IV is constructed by retaining the co-simulation configuration as in Model III, but only replacing the PMSM FEA model with the ECE model, so the parameter settings in the co-simulation configuration remain unchanged.

3.3. Experimental Platform

The set-up of the experimental platform is shown in Figure 8. The target PMSM is driven by the dynamometer to spin at any command speed. The controller is used to control the motor, and a water tank is applied to cool the motor. In the experiment, the parameters of the target motor used in the experiment are introduced in Section 3.1, and the target motor is pulled by the motor, whose rated power is 80 kW.



Figure 8. Experiment bench.

The vector control system described in Model III is applied for driving the test machine. The bus voltage of the system is 540 V and the switching frequency is 5 kHz. The target operating condition chosen for this study is 2200 r/min and 262 Nm, i.e., delivering the peak power at the rated speed.

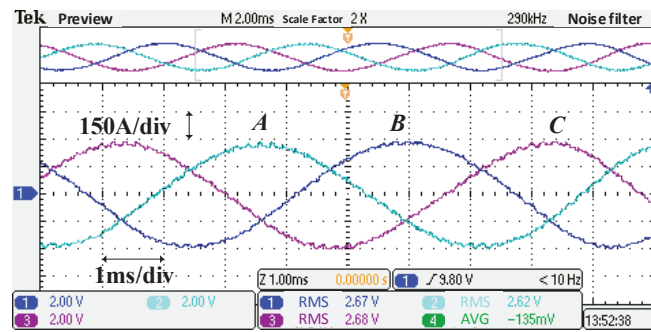
4. Simulation and Experiment Results

In this section, we compare the current harmonics, torque and torque ripple, electromagnetic force, computing time, losses, and efficiency of the four models with simulation and experimental results. Based on the results, we summarize several interesting and important findings of the excitation characteristics.

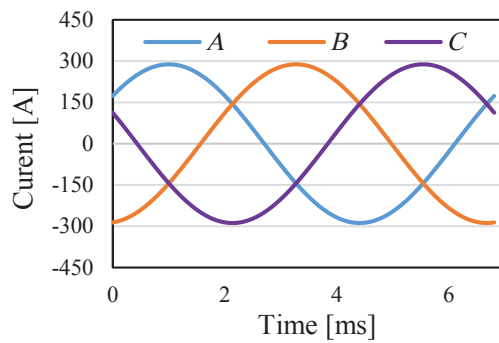
4.1. Comparison of the Current Harmonics

Figure 9 shows the current waveforms in the experiment and the four models at the target operating point. In Figure 9a, each grid on the horizontal axis represents an interval of 1 ms and each grid on the vertical axis represents an interval of 150 A. In Figure 9c–e, the stable period is used to compare their current waveforms. The RMS values of Model I, Model II, Model III, and Model IV are respectively 203.62 A, 202.51 A, 203.48 A, and 203.38 A.

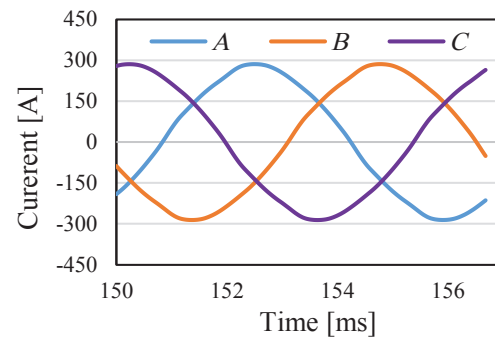
Low-order current harmonics in all models except Model I (no harmonics) are shown in Figure 10a, and high-order current harmonics are compared in Figure 10b. In Figure 10a, apart from the fundamental component, current harmonics appear mainly at the 5th, 7th, 11th, and 13th orders. These components are produced by the voltage source and determined by motor parameters. From Figure 10a, we can see that all the three models have acceptable performances of current harmonics compared with the experimental results, with most differences being less than 10%. Note that the performance of Model IV can be further improved by constructing a more accurate ECE table. The differences between their harmonics for different orders are within 5%, so PWM has little influence on the low-order current harmonics. Overall, Model III is the most precise model for low-order harmonics.



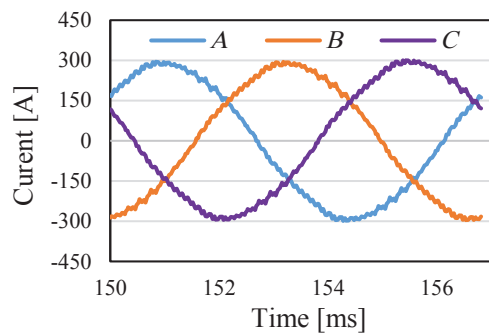
(a) Experimental current waveform.



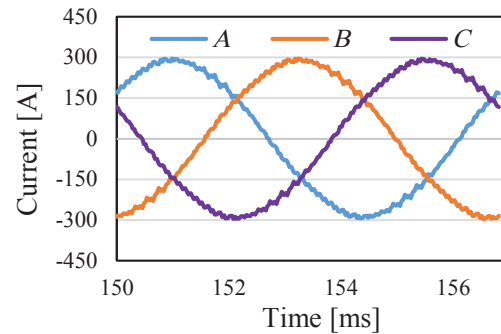
(b) Current waveform of Model I.



(c) Current waveform of Model II.



(d) Current waveform of Model III.



(e) Current waveform of Model IV.

Figure 9. Comparison of current waveforms in different models. (a) Experimental current waveform. (b) Current waveform of Model I. (c) Current waveform of Model II. (d) Current waveform of Model III. (e) Current waveform of Model IV.

For the high-order current harmonics shown in Figure 10b, it can be seen that Model II does not have high-order current harmonics, because it does not include PWM; the high order current harmonics of Model III and IV are very close, but have slight differences from the experimental values, because the experiment incurs the components at many other frequencies.

Total harmonic distortion (*THD*) is a measurement which indicates how much of the distortion of current is due to harmonics in the signal. According to the Equation (7), *THD* values in Model II, Model III, and Model IV are respectively 3.7%, 3.4%, and 3.0%.

$$THD = \sqrt{\frac{I_{RMS}^2 - I_1^2}{I_1^2}}, \quad (7)$$

where I_{RMS} is the RMS value of the current and I_1 is the RMS value of the fundamental component of the current.

According to Figure 10a,b, we can summarize the application of the four models when considering current harmonics. If we do not need to consider the effects of current harmonics, Model I is a better choice; otherwise, Models II, III, and IV are needed. Models II, III, and IV can reflect the motor performance when considering the low-order current harmonics, but only Model III and Model IV reflect the influence of high-order current harmonics on motor performance. For the selection of Model III and Model IV, Model III is more accurate from the perspective of model accuracy, but Model IV is less time-consuming and has a certain accuracy from the perspective of time balance.

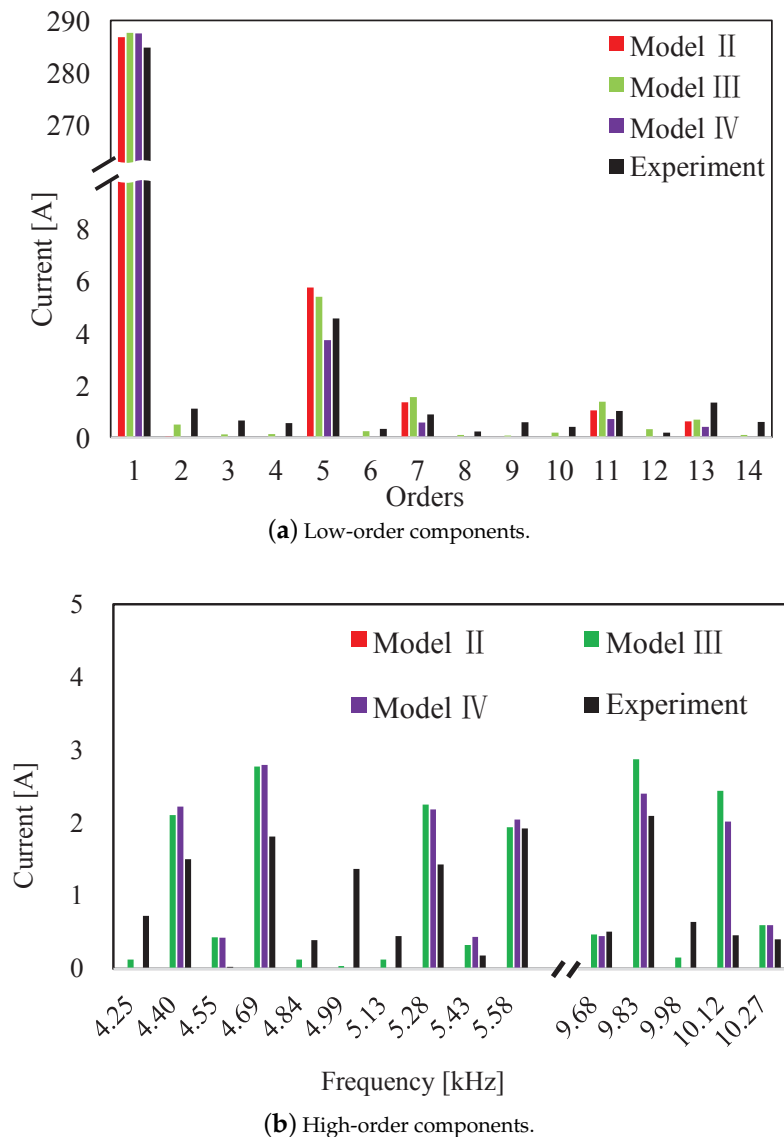


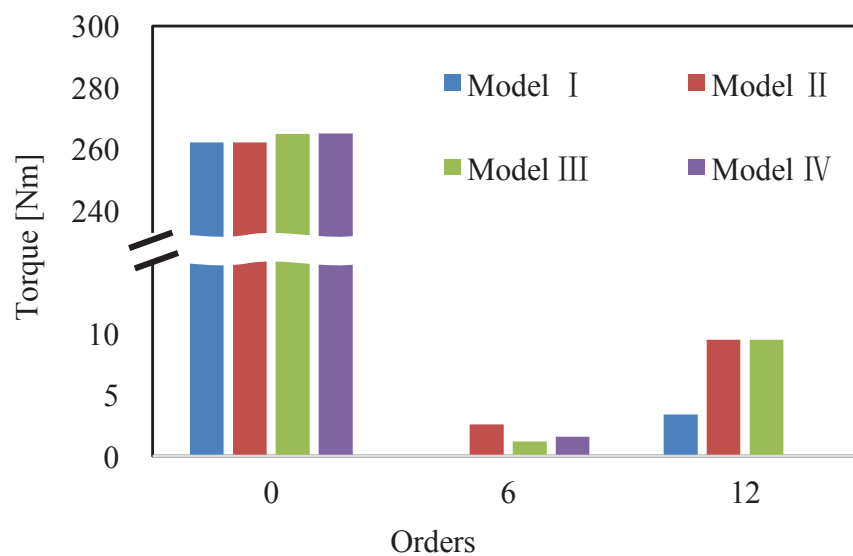
Figure 10. Comparison of current harmonics in different models. (a) Low-order components. (b) High-order components.

4.2. Comparison of Torque and Torque Ripple

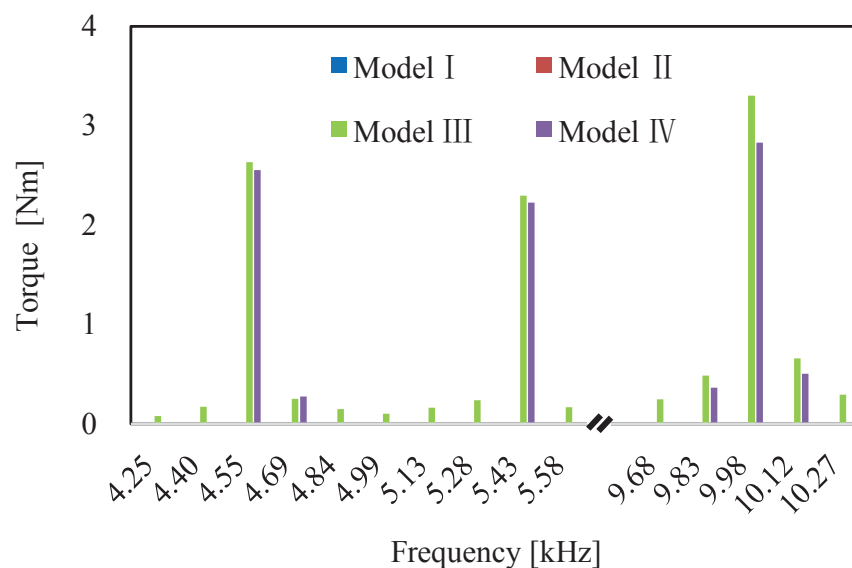
Torque is the integration of the electromagnetic force on the rotor periphery. Current harmonics have influence on the electromagnetic force, and thus indirectly affect the torque ripple.

Since the measured torque in the experiment is the average torque over a period of time rather than the instantaneous value, the harmonic amplitude of the electromagnetic torque in the experiment cannot be obtained. The average torque in the experiment is 262.54 Nm.

The low-order torque harmonics in all models are shown in Figure 11a, while the high-order harmonic components are shown in Figure 11b. The orders of major low-order torque harmonics are times of six—as shown in Figure 11a—because of the 48-slot/8-poles machine configuration. Under sinusoidal current excitation, the 6th-order torque harmonic is low in Model I, which can be ignored. The amplitudes of the 6th-order torque harmonic in Model III and Model IV are close. Model III has more high-order torque harmonics than Model IV; thus, Model III is more accurate than Model IV. Figure 11b shows that the high-order torque harmonics brought by PWM in Model III and Model IV are distributed around times of switching frequencies.



(a) Low-order components.



(b) High-order components.

Figure 11. Comparison of torque harmonics in different models. (a) Low-order components. (b) High-order components.

The torque ripples in all models are shown in Table 2. Torque ripple is the reflection of the influence of current harmonics. Torque ripples are increased in the latter three models because of the additional current harmonics.

Table 2. Comparison of torque ripple ratios in different models.

Models	Torque Ripple Ratio
Model I	2.9%
Model II	8.6%
Model III	14.6%
Model IV	9.0%

4.3. Comparison of Electromagnetic Force

When the radial force varying with time and space is applied to the stator core, the stator core and the base vibrate at the same frequency as the radial force, resulting in deformation. When the frequency of radial force is close to the natural frequency of the machine, resonance can be triggered, causing larger vibration and noise. We calculate the radial electromagnetic force density in several models and make the comparisons between them. Radial electromagnetic force density can be evaluated analytically by the Maxwell Stress Tensor as follows [23]:

$$P_r = \frac{1}{2\mu_0}(B_r^2 - B_t^2), \quad (8)$$

where P_r is the radial electromagnetic force density, B_r and B_t are the radial and tangential component of air-gap flux density, and μ_0 is the permeability of free space.

Figure 12 shows the distribution of radial electromagnetic force density in the middle of the air gap. It can be seen that the distribution of radial electromagnetic force density varies with time and space, and its periodicity is related to the number of poles.

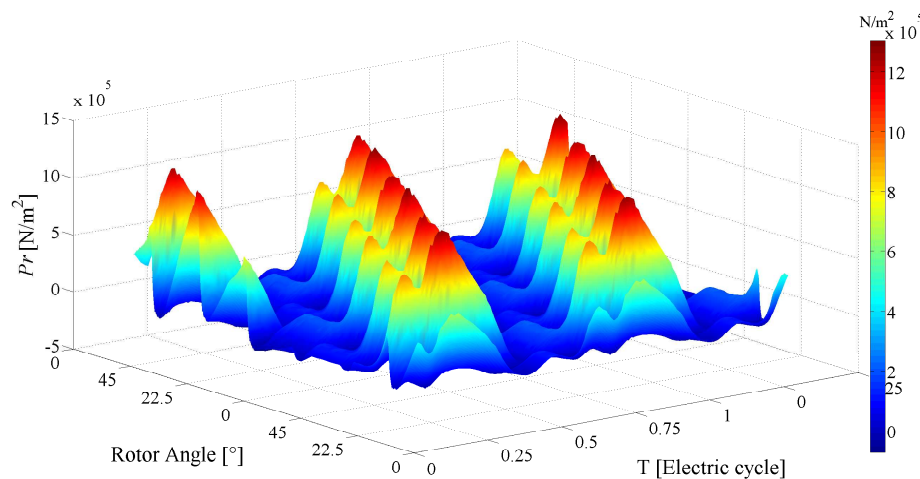


Figure 12. The radial force.

The 2D FFT results of radial electromagnetic force density are shown in Figure 13. The orders of the main harmonics can be written as $(8m, -8 + 48n)$, where the former is the spatial order and the latter is the temporal order. m and n are integers. The radial electromagnetic force densities in the three models have slight differences in the radial electromagnetic force harmonics of the dominant amplitudes, and the amplitudes of the radial electromagnetic force harmonics are mainly dependent on the amplitudes of the current harmonics.

In order to consider the influence of PWM in Model III, the results of the 2D FFT of radial electromagnetic force density considering high-order force harmonics at times of switching frequency 5 kHz are given in Figure 14. In Model III, there are harmonics of radial force density whose frequencies are about 5 and 10 kHz, which are near the carrier frequency and its multiples. Although the amplitude of these harmonics is relatively small, they may approach the natural frequency of the motor and aggravate the vibration noise of the motor. However, these radial electromagnetic force harmonics do not appear in Models I and II without the influence of PWM. Thus, Model III can reflect the electromagnetic force characteristics more accurately compared to Model I.

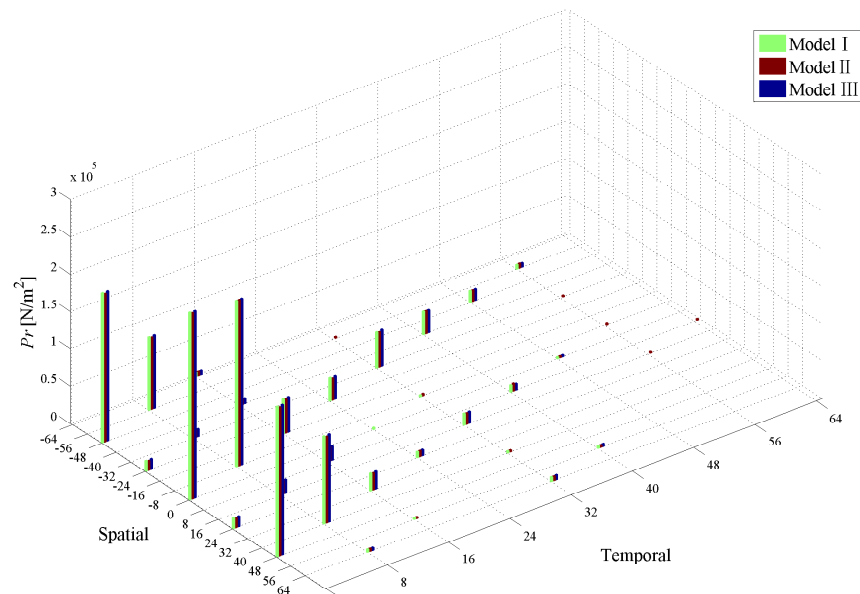


Figure 13. Comparison of 2D FFT results of radial force in three models.

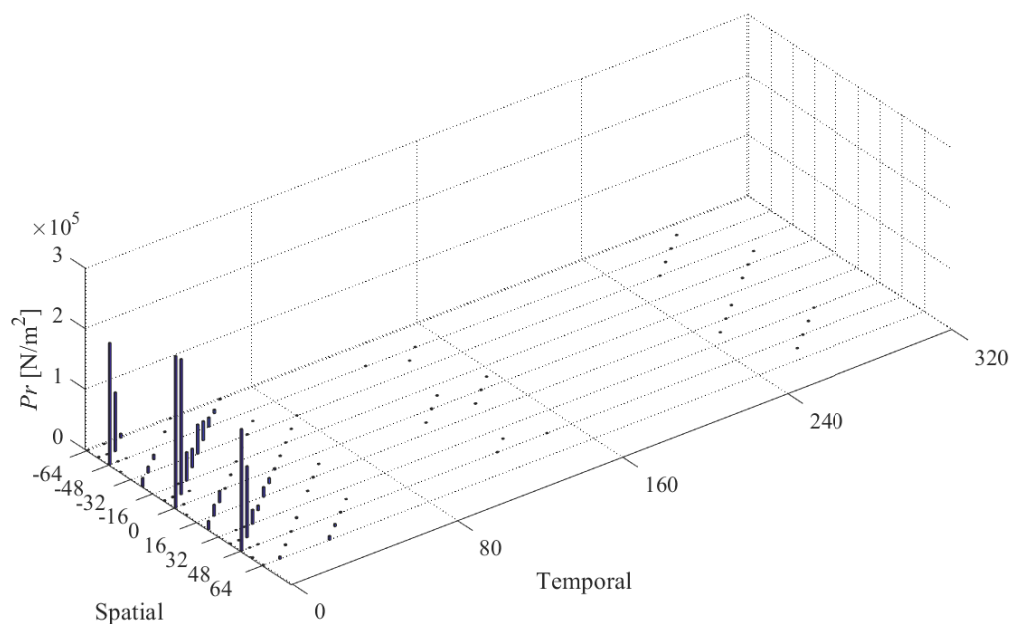


Figure 14. 2D FFT result of radial force in Model III.

4.4. Comparison of Computation Times

It takes two electrical cycles (each electrical cycle at 2200 r/min = 6.818 ms) for Model I and about 200 ms for the other three models to reach steady states in the simulations. The time step is set as 100 steps per electrical cycle in Models I and II, and 1 μ s for Models III and IV, considering the PWM cycle. However, the computation times of all four models may have small changes between different operating points, because the electrical cycles are not fixed and proportional to the motor speed.

Table 3 shows the computation time of one operating point for each model from the initial state to the steady state. From the table, Model I runs fastest, which makes it very popular, and Model III sacrifices too much time, i.e., 1 week on one operating point, for the higher precision. The total computing time of Model IV is composed of two parts. One part is the time in getting the data and setting up the ECE motor model, which takes about four days, with the procedures described in Section 2. Note that the precision of Model IV is dependent on the accuracy of the ECE table. Once the ECE model is constructed, it can be used throughout the whole motor operating region. The other part is the time for simulating Model IV, where the machine drive is linked with the ECE motor model. It takes about 10 min with a 1 μ s time step for each operating point.

Table 3. Comparison of approximate computing times in different models.

Models	Computing Time
Model I	10 min
Model II	6 h
Model III	1 week
Model IV	10 min
ECE look-up table	4 days

4.5. Comparison of Losses and Efficiency

In this study, the core loss and PM loss are calculated by finite element software, while the copper loss is evaluated using DC resistance. Because the ECE in Model IV is not capable of predicting machine core loss and PM loss directly, the currents of the stable state in Model IV are exported and set to be the excitation of the FEA motor model to analyze the losses.

In Table 4, it can be observed that the iron loss in Model III and Model IV increases obviously because of the consideration of the current harmonics, and because the copper loss in the models also increases a small amount. The effect of different excitations on PM loss is very large, as the PM loss grows about 10 times more in Model III than in Model I. This is likely to result in high temperatures and demagnetization of PMs. The loss values of Model IV and Model III are close to each other, which means that in representing losses, Model III can be replaced by Model IV.

Table 4. Comparison of losses in different models.

Loss	Model I	Model II	Model III	Model IV
DC copper loss [W]	4764.6	4645.3	4829.4	4833.0
Core loss [W]	706.9	752.2	804.6	783.4
PM loss [W]	4.8	3.0	49.5	36.4
Total loss [W]	5476.3	5400.5	5683.5	5652.8

Figure 15 shows the efficiency map of the target motor in simulations and experiments. Here, we map the efficiency of Model I and Model IV, because Model IV has a very close performance to that of Model III, and has better accuracy than that of Model II, especially in representing the current harmonics. With an ideal sinusoidal current source, the maximum efficiency is about 97.2%, as shown in Figure 15a. Figure 15b shows the efficiency map of the motor in Model IV. Compared with Model I,

the maximum efficiency region is unchanged, but the efficiency of this region is reduced by about 1%, and the maximum efficiency is 96.78%. The experimental motor efficiency map is shown in Figure 15c. Compared with the simulation results, the range of the maximum efficiency region (higher than 95%) is reduced, and the maximum efficiency is 95.92%. Overall, the efficiency of the experiment is about 1% lower than that of Model IV, mainly because the mechanical loss is not considered in the simulation results. Thus, Model III and Model IV are more accurate than Model I when calculating losses.

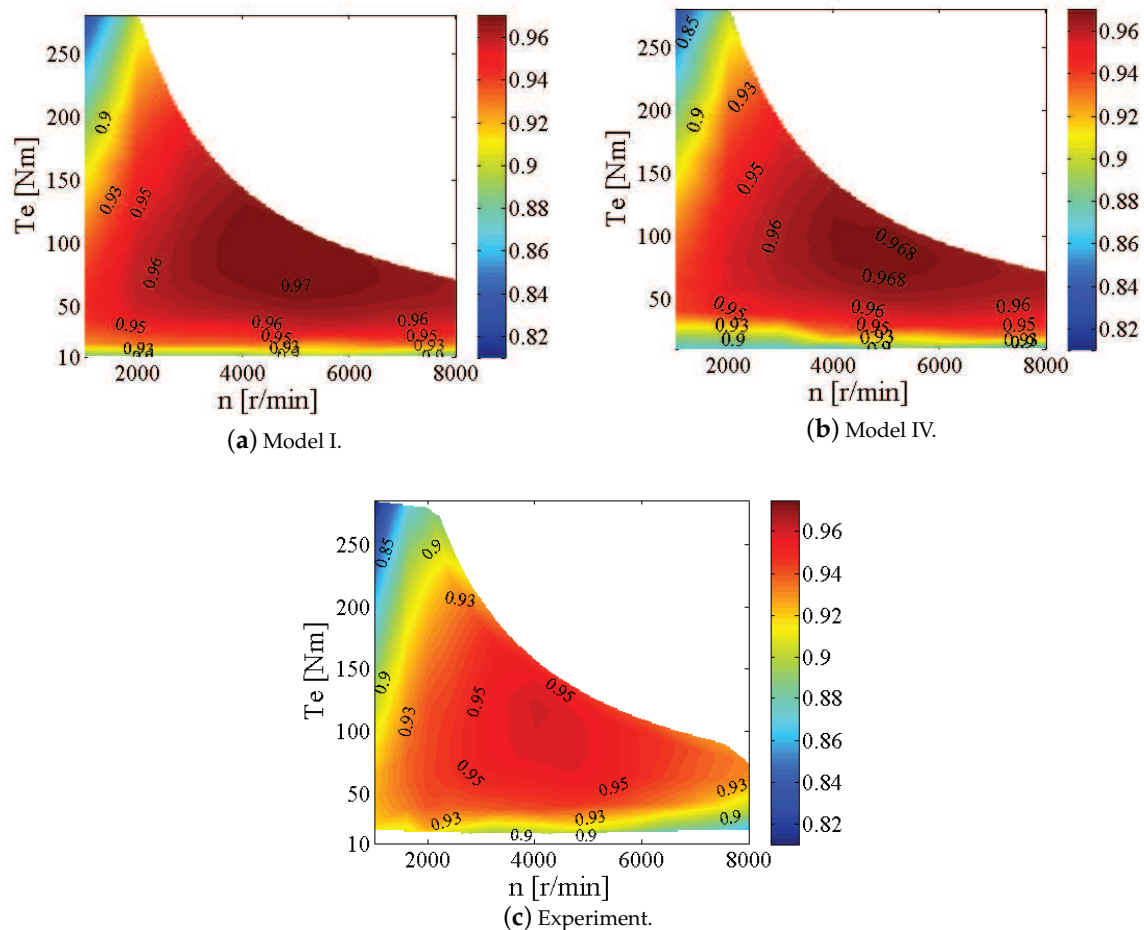


Figure 15. Efficiency map of (a) Model I, (b) Model IV, and (c) the experiment.

4.6. Summary of Comparisons between Models

Based on the results from Sections 4.1 and 4.5, we can make a summary of the excitation characteristics of the four models:

1. Overall, Model III has the best performance for the motor drive system because it has more details of the excitation sources, especially the current harmonics. Model IV also has a very close performance to that of Model III, mainly because its excitation source includes the most important components of the current harmonics in Figure 10. All other models have better performances than that of Model I, which indicates that the excitations are very crucial to the complete motor drive system, and the more accurate the excitations are, the better the system performance will be.
2. Based on the excitation characteristics, Model IV is a very good substitution for Model III in several significant aspects of the motor, and more importantly, Model IV saves a great amount of time—as shown in Table 3—even considering the additional time for calculating losses, usually several hours for the entire operating region.

3. Because it has the shortest simulation time, Model I is especially useful to quickly learn the performance of a motor at the initial design stage with acceptable accuracy. However, it does not provide any information on current harmonics.
4. Model II shows similar low-order current harmonics to those of Model III. On the other hand, the computing time of Model II is less than that of Model III, but longer than that of Model IV. Model II can be adopted to simulate some typical situations, such as evaluating the effects of rotor eccentricity.

5. Conclusions

In this paper, four machine/drive systems with different excitation sources have been modeled and simulated, and their characteristics were investigated. We find that the excitations that can quickly and accurately reflect the actual system performance by comparing the performances of different models. The current harmonics, torque, electromagnetic force, computation time, and efficiency are analyzed and compared among these models and experiments. The experiment demonstrates that Model III allows the most precise study of the considered system. Model IV is a good substitution, providing similar results with a shorter running time. The distribution characteristics of electromagnetic force can also be used for further research on the NVH of the motors, which is especially important for EVs.

Author Contributions: W.J. conceived and designed the study. Q.G. and Z.Z. gave suggestions and revised the manuscript.

Funding: This research was funded under the Fundamental Research Funds for the Central Universities (Award NJ2018004) and supported by National Key Laboratory of Science and Technology on Helicopter Transmission (Nanjing University of Aeronautics and Astronautics) (Award HTL-O-19G12) and National Natural Science Foundation of China under Award 51607088.

Acknowledgments: The authors are grateful to the JSOL Corp. for making their JMAG software available for this investigation.

Conflicts of Interest: The authors declare no conflict of interest.

References

1. Zhu, Z.Q.; Howe, D. Electrical machines and drives for electric, hybrid, and fuel cell vehicles. *Proc. IEEE* **2007**, *95*, 746–765. [\[CrossRef\]](#)
2. Rahman, K.; Jurkovic, S.; Savagian, P.J.; Patel, N.; Dawsey, R. Retrospective of electric machines for EV and HEV traction applications at general motors. In Proceedings of the 2016 IEEE Energy Conversion Congress and Exposition (ECCE), Milwaukee, WI, USA, 18–22 September 2016; pp. 1–8.
3. Nozawa, S.; Maekawa, T.; Yagi, E.; Terao, Y.; Kohno, H. Development of new power control unit for compact-class vehicle. In Proceedings of the 2010 22nd International Symposium on Power Semiconductor Devices & IC's (ISPSD), Hiroshima, Japan, 6–10 June 2010.
4. Yoshinori, S.; Shigeaki, I.; Takahito, O. Development of High Response Motor and Inverter System for the Nissan LEAF Electric Vehicle. In Proceedings of the SAE 2011 World Congress, Detroit, MI, USA, 12–14 April 2011.
5. Nakada, T.; Ishikawa, S.; Oki, S. Development of an Electric Motor for a Newly Developed Electric Vehicle. In Proceedings of the SAE World Congress, Detroit, MI, USA, 8–10 April 2014.
6. John M. M. *Oak Ridge National Laboratory Annual Progress Report for the Power Electronics and Electric Motors Program*; Oak Ridge National Laboratory: Oak Ridge, TN, USA, 2013.
7. Momen, F.; Rahman, K.; Son, Y. Electrical Propulsion System Design of Chevrolet Bolt Battery Electric Vehicle. *IEEE Trans. Ind. Appl.* **2019**, *55*, 376–384. [\[CrossRef\]](#)
8. Pillay, P.; Krishnan, R. Modeling, Simulation, and Analysis of Permanent-Magnet Motor Drives, Part I: The Permanent-Magnet Synchronous Motor Drive. *IEEE Trans. Ind. Appl.* **1989**, *25*, 265–273. [\[CrossRef\]](#)
9. Singh, S.; Tiwari, A.N. Analysis and simulation of vector controlled PMSM drive using SVPWM inverter. In Proceedings of the 2017 2nd International Conference for Convergence in Technology (I2CT), Mumbai, India, 7–9 April 2017; pp. 709–714.

10. Gupta, A.K.; Khambadkone, A.M. A Space Vector PWM Scheme for Multilevel Inverters Based on Two-Level Space Vector PWM. *IEEE Trans. Ind. Electron.* **2006**, *53*, 1631–1639. [[CrossRef](#)]
11. Yamazaki, K.; Watari, S. Loss analysis of permanent-magnet motor considering carrier harmonics of PWM inverter using combination of 2-D and 3-D finite-element method. *IEEE Trans. Magn.* **2005**, *41*, 1980–1983. [[CrossRef](#)]
12. Estima, J.O.; Marques Cardoso, A.J. Efficiency Analysis of Drive Train Topologies Applied to Electric/Hybrid Vehicles. *IEEE Trans. Veh. Technol.* **2012**, *61*, 1021–1031. [[CrossRef](#)]
13. Yamazaki, K.; Abe, A. Loss Investigation of Interior Permanent-Magnet Motors Considering Carrier Harmonics and Magnet Eddy Currents. *IEEE Trans. Ind. Appl.* **2009**, *45*, 659–665. [[CrossRef](#)]
14. Wang, X.; Zhou, W.; Dou, R. Analysis of Harmonic Current in Permanent Magnet Synchronous Motor and Its Effect on Motor Torque. *J. Electromagn. Anal. Appl.* **2012**, *4*, 15–20. [[CrossRef](#)]
15. Miyama, Y.; Hazeyama, M.; Hanioka, S.; Watanabe, N.; Daikoku, A.; Inoue, M. PWM Carrier Harmonic Iron Loss Reduction Technique of Permanent-Magnet Motors for Electric Vehicles. *IEEE Trans. Ind. Appl.* **2016**, *52*, 2865–2871. [[CrossRef](#)]
16. Xu, Y.; Yuan, Q.; Zou, J.; Yao, Y.; Zhu, G. Sinusoidal periodic carrier frequency modulation in reducing electromagnetic noise of permanent magnet synchronous motor. *IET Electric Power Appl.* **2013**, *7*, 223–230. [[CrossRef](#)]
17. Accardo, L.; Fioretto, M.; Giannini, G.; Marino, P. Techniques of PWM space vector modulation for the reduction of magnetic acoustic noise in traction motor. In Proceedings of the International Symposium on Power Electronics, Electrical Drives, Automation and Motion, Taormina, Italy, 23–26 May 2006; pp. 1084–1089.
18. Liang, W.; Wang, J.; Luk, P.C.K.; Fang, W.; Fei, W. Analytical Modeling of Current Harmonic Components in PMSM Drive With Voltage-Source Inverter by SVPWM Technique. *IEEE Trans. Energy Convers.* **2014**, *29*, 673–680. [[CrossRef](#)]
19. Ansys. Equivalent Circuit Extraction (ECE) Model for Motor. Available online: <https://wenku.baidu.com/view/935c4cd159f5f61fb7360b4c2e3f5727a5e9249c.html> (accessed on 1 June 2019).
20. Available online: <http://bbs.simol.cn/forum.php?mod=viewthread&tid=124046&fromuid=248715> (accessed on 1 June 2019).
21. del Blanco, F.B.; Degner, M.W.; Lorenz, R.D. Dynamic analysis of current regulators for AC motors using complex vectors. *IEEE Trans. Ind. Appl.* **1999**, *35*, 1424–1432. [[CrossRef](#)]
22. Briz, F.; Degner, M.W.; Lorenz, R.D. Analysis and design of current regulators using complex vectors. *IEEE Trans. Ind. Appl.* **2000**, *36*, 817–825. [[CrossRef](#)]
23. Li, Y.; Chai, F.; Song, Z.; Li, Z. Analysis of Vibrations in Interior Permanent Magnet Synchronous Motors Considering Air-Gap Deformation. *Energies* **2017**, *10*, 1259. [[CrossRef](#)]

